ARTICLE   Open Access

Self-cleaning semiconductor heterojunction substrate: ultrasensitive detection and photocatalytic degradation of organic pollutants for environmental remediation

Mingyue Hu[1,2,3], Yingnan Quan[1,2,3], Shuo Yang[4], Rui Su[5], Huilian Liu[1,2,3], Ming Gao [1,2,3], Lei Chen[1,2,3] and Jinghai Yang[1,2,3]

Abstract

Emerging technologies in the field of environmental remediation are becoming increasingly significant owing to the increasing demand for eliminating significant amounts of pollution in water, soil, and air. We designed and synthesized MoS_2/Fe_2O_3 heterojunction nanocomposites (NCs) as multifunctional materials that are easily separated and reused. The trace detection performance of the prepared sample was examined using bisphenol A (BPA) as the probe molecule, with limits of detection as low as 10^{-9} M; this detection limit is the lowest among all reported semiconductor substrates. BPA was subjected to rapid photocatalytic degradation by MoS_2/Fe_2O_3 NCs under ultraviolet irradiation. The highly recyclable MoS_2/Fe_2O_3 NCs exhibited photo-Fenton catalytic activity for BPA and good detection ability when reused as a surface-enhanced Raman scattering (SERS) substrate after catalysis. The SERS and photocatalysis mechanisms were proposed while considering the effects of the Z-scheme charge-transfer paths, three-dimensional flower-like structures, and dipole–dipole coupling. Moreover, the prepared MoS_2/Fe_2O_3 NCs were successfully applied in the detection of BPA in real lake water and milk samples. Herein, we present insights into the development of MoS_2/Fe_2O_3 materials, which can be used as multifunctional materials in chemical sensors and in photocatalytic wastewater treatments for the removal of recalcitrant organic pollutants.

Introduction

Serious environmental pollution and accelerated global warming are attributed to the rapid consumption of fossil fuels, the increasing population, and the rapid development of the economy. Thus, the development of innovative and renewable environmental remediation materials is becoming increasingly important[1–6]. Since mechanically exfoliated graphene was discovered, the development of

two-dimensional (2D) materials consisting of atomically thin crystal layers bound by van der Waals forces has accelerated owing to the potential applications of these materials in optoelectronics, catalysis, new technologies, and electricity[7–9]. 2D-MoS_2 nanosheets are excellent layered materials, having unique layered structures and large surface areas. It is important to investigate methods for improving the chemical properties of MoS_2, which may affect its application in electronic devices, catalysis, and molecular sensing[10]. A popular method for improving the properties of MoS_2 is the decoration of MoS_2 with noble metal nanoparticles. For instance, a MoS_2/noble metal nanoparticle composite can induce local surface plasmon resonance (LSPR) for activating the photoelectrocatalysis of H_2 and enhancing the light absorption or emission of

Correspondence: Ming Gao (gaomingphy@126.com) or
Lei Chen (chenlei@jlnu.edu.cn) or Jinghai Yang (jhyang1@jlnu.edu.cn)
[1]Key Laboratory of Functional Materials Physics and Chemistry of the Ministry of Education, Jilin Normal University, 130103 Changchun, People's Republic of China
[2]National Demonstration Centre for Experimental Physics Education, Jilin Normal University, 136000 Siping, People's Republic of China
Full list of author information is available at the end of the article

MoS$_2$. Moreover, the LSPR can generate surface-enhanced Raman scattering (SERS), which can be used in biological and chemical sensing applications[11–13]. Among various traditional noble metal materials, Au nanomaterials are the most widely used SERS substrate material[14–16]. However, the high cost and specialized instruments required for Au substrates hinder their practical application. Due to its very high SERS activity, Ag is another widely studied substrate material[17]. Although the price of Ag is much lower than the price of Au, the main defect of Ag is its poor stability, which easily oxidizes in air. To address these problems, it is essential to exploit synergistic effects by incorporating inexpensive and stable semiconductors.

Thus far, a few MoS$_2$-based heterostructures, such as CdS/MoS$_2$, TiO$_2$/MoS$_2$, and MoO$_3$/MoS$_2$, have exhibited higher photocatalytic efficiencies than pristine MoS$_2$[18–20]. Investigations have been continuously conducted on the efficient separation of a nanocomposite (NC) from a treated effluent, along with the subsequent reusability of the NC. Several research groups have begun to focus on magnetically separable photocatalysts for wastewater treatment, demonstrating the value of the special properties of magnetic materials. Among these magnetic materials, Fe$_2$O$_3$ has a narrow bandgap, high chemical resistance, and high resistance to corrosion. Therefore, rationally designed MoS$_2$/Fe$_2$O$_3$ NCs can serve as a reusable SERS substrate for detection and easily reclaimed photocatalyst. The recovery and economical reuse of MoS$_2$/Fe$_2$O$_3$ NCs photocatalysts is easily achieved by adding an external magnetic field.

Bisphenol A (BPA) is believed to be an endocrine disruptor and widely exists in food containers and the environment. Even low levels of BPA entering the body can disrupt the endocrine system by binding to estrogen receptors, which may lead to cardiovascular diseases, immune function deficiencies, impaired reproductive capacity, and other diseases[21–23]. Thus, it is imperative to develop a facile, rapid, and inexpensive method for BPA detection and degradation.

In this study, MoS$_2$/Fe$_2$O$_3$ NCs were prepared via a simple low-temperature hydrothermal method, and the advantages of the two materials were combined. For example, after 50 min of ultraviolet (UV) irradiation, the substrate completely degraded BPA, and upon recovery, demonstrated its detection capability. Compared with MoS$_2$ NFs and Fe$_2$O$_3$ NPs, the rate of degradation of BPA and the SERS activity of MoS$_2$/Fe$_2$O$_3$ NCs were significantly better. This new, easily recoverable SERS sensor with a high sensitivity will facilitate sensing harmful molecules. To the best of our knowledge, no MoS$_2$/Fe$_2$O$_3$ composites that exhibit BPA detection and photocatalysis multifunctionality have been reported thus far. Photocatalytic and SERS mechanisms were also proposed.

Results and discussion
Characterization analysis of MoS$_2$/Fe$_2$O$_3$ NCs

A growth flow diagram of the MoS$_2$/Fe$_2$O$_3$ NCs is shown in Fig. 1. Figure 2a confirms that the MoS$_2$ sample was pure hexagonal 2H-MoS$_2$ (JCPDS card no. 37-1492). The peak with the highest intensity (at $2\theta = 14.09°$) indicated that MoS$_2$ had excellent lamellar growth in the *c*-axis direction. In regard to MoS$_2$/Fe$_2$O$_3$, some of the peaks corresponded to 2H-MoS$_2$, while others corresponded to tetragonal γ-Fe$_2$O$_3$ (JCPDS card no. 39-1346) phase, indicating that the native structure of each constituent was well preserved during the reaction. The intensities of the MoS$_2$ peaks for the MoS$_2$/Fe$_2$O$_3$ NCs were lower than those for pure MoS$_2$ because the Fe$_2$O$_3$ NPs attached to the MoS$_2$ nanoflowers (NFs). Raman spectra confirmed the chemical composition of the MoS$_2$/Fe$_2$O$_3$ NCs and MoS$_2$. Two characteristic Raman peaks of MoS$_2$ were observed at 337 and 377 cm^{-1}, corresponding to the A_{1g} and $^1E_{2g}$ vibration modes, respectively; additionally, their peak frequency difference was $\Delta k = 40$ cm^{-1} (Fig. 2b)[24–26]. However, after the incorporation of Fe$_2$O$_3$, the characteristic Raman peaks of MoS$_2$ shifted to 338 and 379 cm^{-1}, and the peak frequency difference was $\Delta k = 41$ cm^{-1}. Δk represents the number of
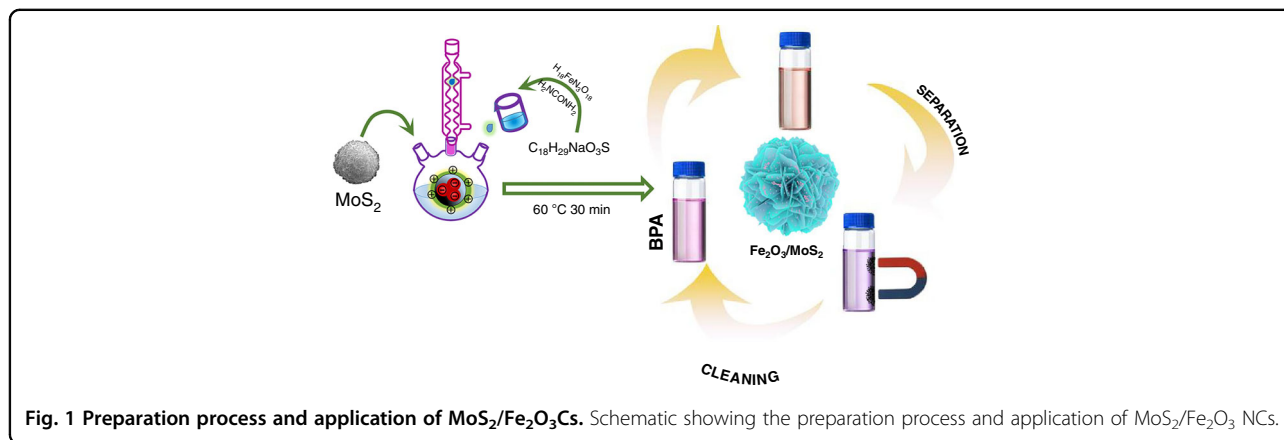
Fig. 1 Preparation process and application of MoS$_2$/Fe$_2$O$_3$Cs. Schematic showing the preparation process and application of MoS$_2$/Fe$_2$O$_3$ NCs.

Fig. 2 Structural quality and morphology of MoS$_2$/Fe$_2$O$_3$ NCs. a XRD patterns of MoS$_2$ and MoS$_2$/Fe$_2$O$_3$. **b** Raman spectra of MoS$_2$ and MoS$_2$/Fe$_2$O$_3$. **c** SEM images of MoS$_2$ NFs. **d** TEM image of typical MoS$_2$ NFs. **e** SEM image of Fe$_2$O$_3$ NPs. **f** TEM image of the Fe$_2$O$_3$ NPs. **g** SEM image of MoS$_2$/Fe$_2$O$_3$ NCs. **h** HRTEM image of MoS$_2$/Fe$_2$O$_3$ NCs. **i–m** Typical STEM image of MoS$_2$/Fe$_2$O$_3$ and the corresponding elemental mapping images of Mo, S, Fe, and O.

MoS$_2$ layers[27]. As shown in Fig. 2c, the pristine MoS$_2$ samples were flower-like nanospheres with diameters of ~1–2 μm. Wrinkles and scrolling were observed in the transmission electron microscopy (TEM) images (Fig. 2d), indicating the extremely small thickness of the 2D structure. Scanning electron microscope (SEM) (Fig. 2e) revealed the presence of Fe$_2$O$_3$ nanoparticles (well below 20 nm in size according to TEM, Fig. 2f). As shown in Fig. 2g, Fe$_2$O$_3$ nanoparticles were dispersed, and a few Fe$_2$O$_3$ nanoparticle aggregations were present on the MoS$_2$ NF. The high-resolution TEM image in Fig. 2h provided further insight regarding the morphology and microstructure of MoS$_2$/Fe$_2$O$_3$. The *d*-spacing of the lattice stripes of Fe$_2$O$_3$ was 0.252 nm, which corresponded to the (0 0 1) lattice plane of hexagonal Fe$_2$O$_3$[28]. In regard to the MoS$_2$/Fe$_2$O$_3$ NCs, the lattice spacing was 0.624 nm, corresponding to the hexagonal MoS$_2$ (0 0 2) plane. In addition, the boundary between Fe$_2$O$_3$ and MoS$_2$ was clearly observed, indicating that a heterojunction was formed between these two components. The regions with different colors in Fig. 2j–m correspond to S, Mo, Fe, and O, and the elemental distribution in MoS$_2$/Fe$_2$O$_3$ was uniform.

X-ray photoelectron spectroscopy (XPS) was performed to analyze the electronic states and chemical composition of the MoS$_2$/Fe$_2$O$_3$ NCs (Fig. 3). The survey scan spectra of pristine MoS$_2$, Fe$_2$O$_3$, and MoS$_2$/Fe$_2$O$_3$ NCs are presented in Fig. 3a, which confirmed the coexistence of Fe 2p, O 1s, Mo 3p, and S 2p in the hybrid. The Mo 3d spectra exhibited three peaks for pristine MoS$_2$, but after forming the MoS$_2$/Fe$_2$O$_3$ NCs, four peaks appeared in Fig. 3b. The peaks at 235.8, 232.6, 229.4, and 226.5 eV corresponded to Mo^{6+} 3$d_{3/2}$, Mo^{4+} 3$d_{3/2}$, Mo^{4+} 3$d_{5/2}$, and S 2s, respectively. A small portion of Mo^{4+} was oxidized into Mo^{6+} during the reaction, confirming that Fe$_2$O$_3$ was successfully recombined with MoS$_2$. In Fig. 3b, the two peaks at 163.3 and 162.2 eV could be assigned to the doublet S 2$p_{1/2}$ and S 2$p_{3/2}$ orbitals of divalent sulfide ions (S^{2-}), respectively, in agreement with the formation of the MoS$_2$ nanostructure[29]. The Fe 2p spectrum exhibited two peaks at 710.4 and 723.7 eV (Fig. 3c), corresponding to the Fe 2$p_{3/2}$ and Fe 2$p_{1/2}$ components of γ-Fe$_2$O$_3$[30]. XPS peak shifts were also observed in the MoS$_2$/Fe$_2$O$_3$ composites compared with pristine Fe$_2$O$_3$, confirming the successful formation of an electronically coupled interface between MoS$_2$ and Fe$_2$O$_3$[31,32]. The high-resolution O 1s spectrum of the MoS$_2$/Fe$_2$O$_3$ NCs is shown in Fig. 3d. The spectrum could be deconvoluted into two components: the peak at 529.3 eV was related to

Fig. 3 The electronic states and chemical composition of the MoS₂/Fe₂O₃ NCs. a XPS survey spectra for MoS₂/Fe₂O₃ NCs, MoS₂, and Fe₂O₃. XPS spectra of MoS₂/Fe₂O₃ and MoS₂: **b** Mo 3d, **c** S 2p, **d** Fe 2p, **e** O 1s, and **f** C 1s of the MoS₂/Fe₂O₃ NCs.
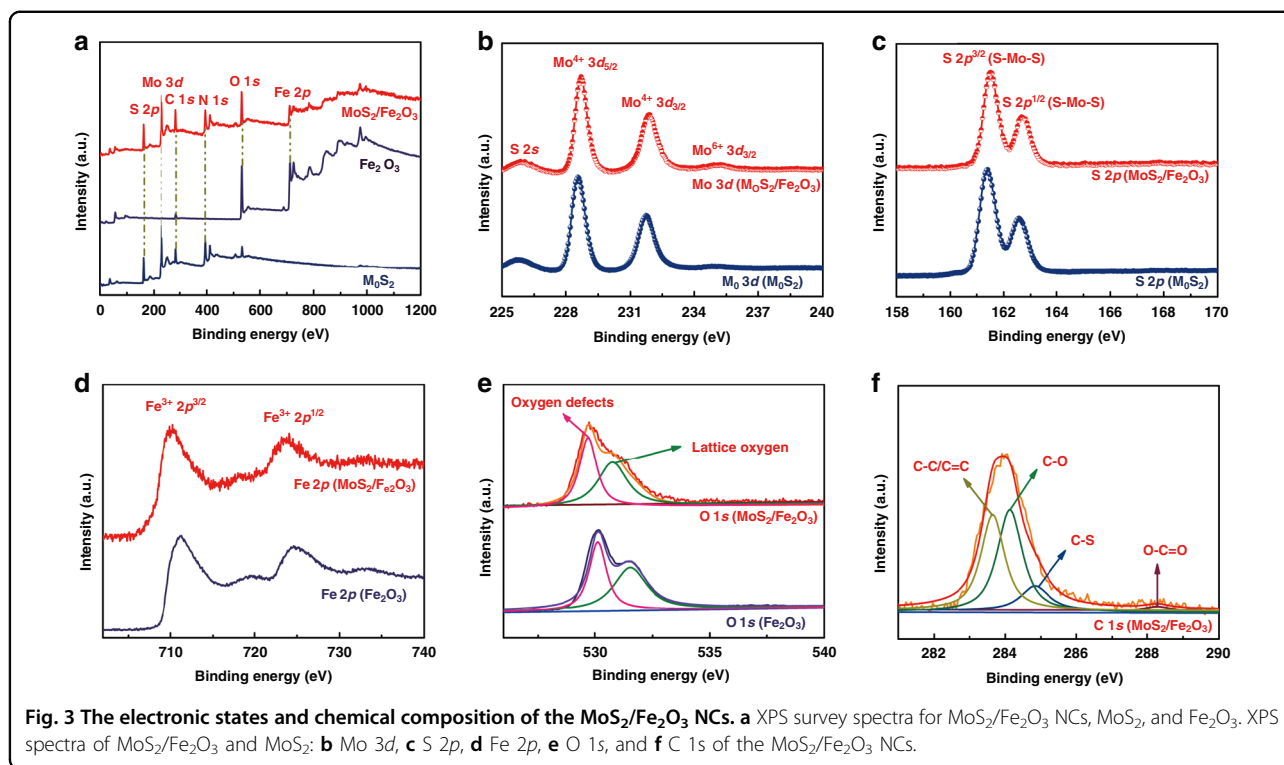
the binding energy of Fe-O in Fe_2O_3 caused by lattice O, and the peak at 530.7 eV was related to the O^{2-} ions in the anoxic region[33]. Specifically, the C 1s spectrum (Fig. 3f) was deconvoluted into four peaks at 283.7, 284.1, 284.9, and 288.3 eV corresponding to the C-C/C = C, C-O, C-S, and O-C = O bonds, respectively[34].

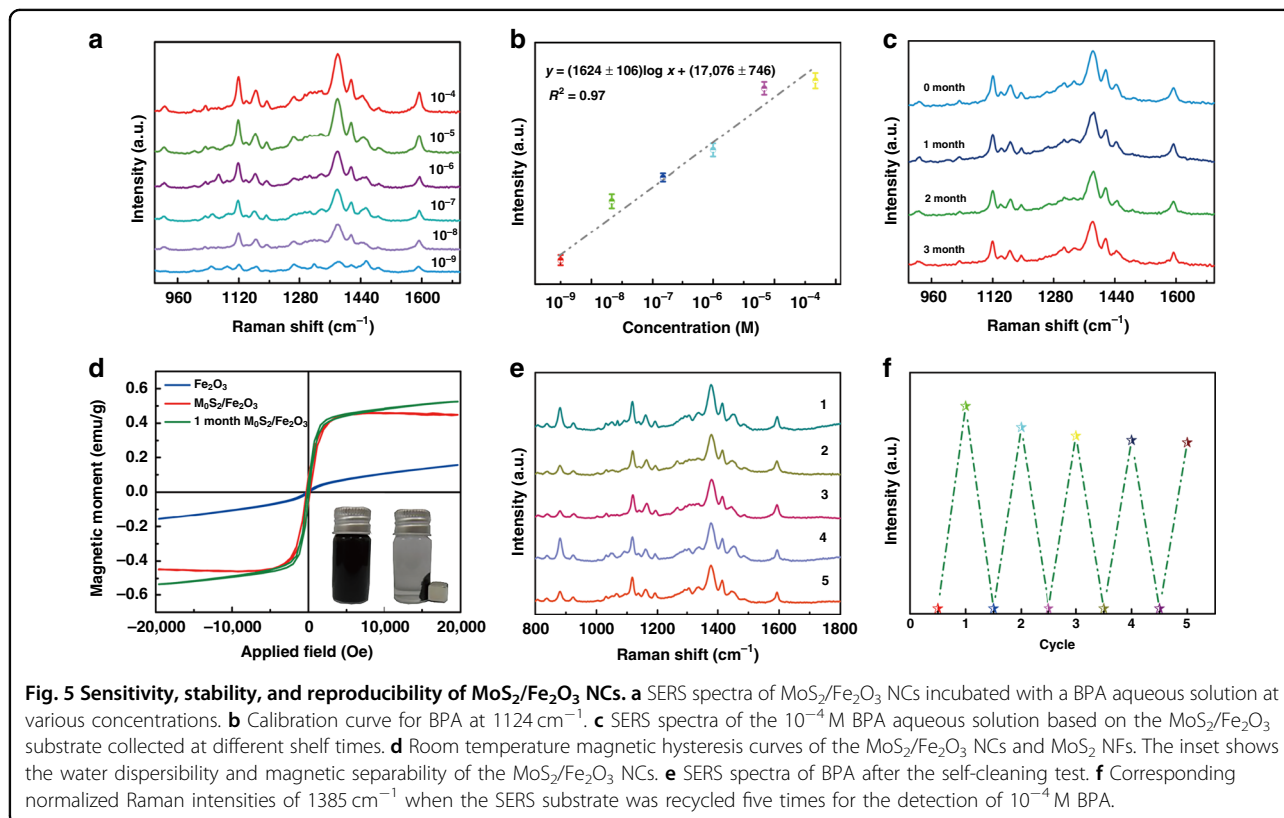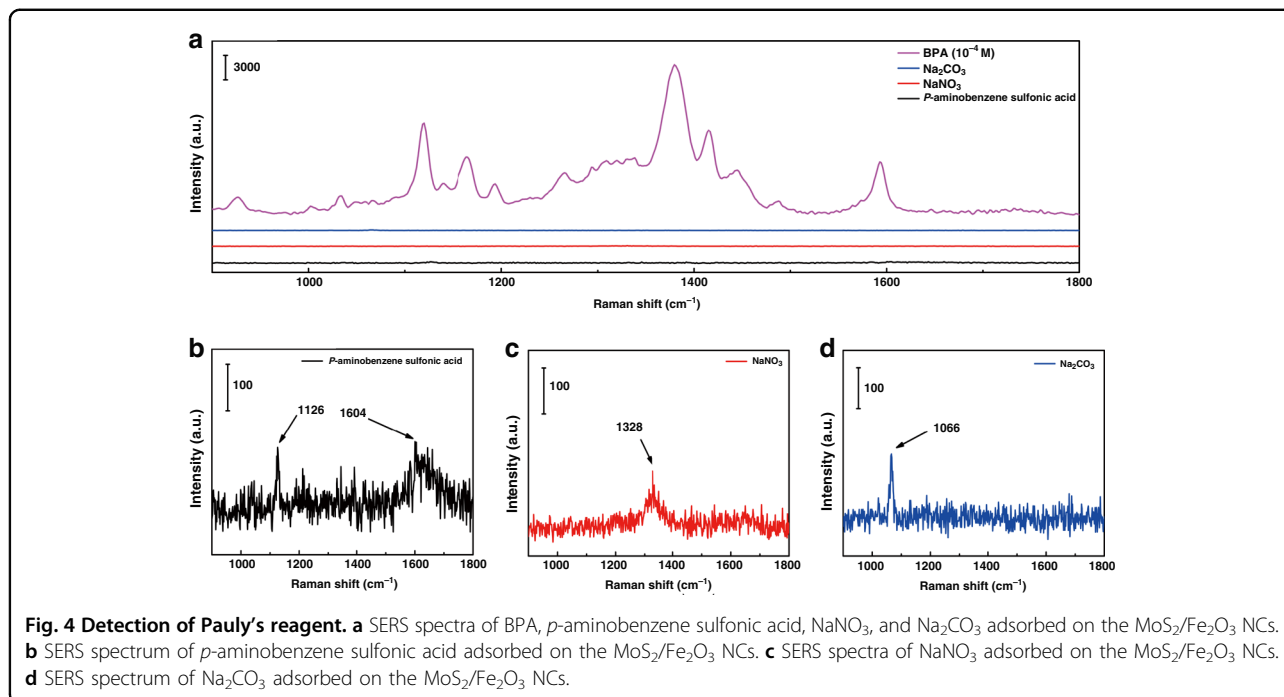## SERS enhancement and reusability of MoS₂/Fe₂O₃ NCs for BPA detection

Herein, *p*-aminobenzene sulfonic acid, $NaNO_3$, and Na_2CO_3 as Pauly's reagent were added in the BPA detection test to enhance the adhesion of BPA on the surface of the MoS₂/Fe₂O₃ NCs. As shown in Fig. 4, *p*-aminobenzene sulfonic acid, $NaNO_3$ and Na_2CO_3, were all low Raman scattering active molecules; therefore, their addition had almost no effect on BPA detection. To confirm that MoS₂/Fe₂O₃ had excellent SERS properties, SERS spectra of BPA absorbed on MoS₂/Fe₂O₃ at various concentrations ranging from 10^{-4} to 10^{-9} M were obtained, as shown in Fig. 5a. These results indicated that as the concentration of BPA decreased, the intensity of the Raman peaks decreased. The characteristic peak of BPA at $1124 \, cm^{-1}$ was observed at concentrations as low as 10^{-9} M, indicating that the MoS₂/Fe₂O₃ NCs had a high sensitivity. The intensity of the peak at $1124 \, cm^{-1}$ was correlated with the BPA concentration; thus, we used it for further quantitative analysis. Figure 5b shows the direct proportionality between the BPA concentration, in the range of 10^{-4}–10^{-9} M, and the normalized Raman

signal intensity. The linear equation is as follows:

$$\log(I_{1124}) = (1624 \pm 106)\log C_{BPA} + (17{,}076 \pm 746) \tag{1}$$

with a squared correlation coefficient of $R^2 = 0.97$. The stability of the substrate is an important factor that must be considered. As shown in Fig. 5c, the SERS spectrum of the MoS₂/Fe₂O₃ NCs substrate hardly changed over time; thus, the MoS₂/Fe₂O₃ NCs could be stored for at least 3 months under ambient conditions.

As shown in Fig. 5d, the hysteresis loop of the MoS₂/Fe₂O₃ NCs indicated excellent superparamagnetic behavior. The saturation magnetization (M_s) value of the MoS₂/Fe₂O₃ NCs (0.46 emu/g) was higher than that of Fe₂O₃ alone. This good magnetic property completely satisfied the requirements for magnetic separation. The uniformly dispersed MoS₂/Fe₂O₃ NCs quickly separated from the solution and formed aggregates within 22 s when external magnets were used. Conversely, when the magnets were removed, the agglomerated MoS₂/Fe₂O₃ quickly redistributed into the solution via slight shaking, as shown in the inset of Fig. 5d. In addition, we measured the magnetization of the MoS₂/Fe₂O₃ NCs after 3 months and found that the M_s value hardly changed (from 0.46 to 0.52 emu/g). Hence, we concluded that MoS₂/Fe₂O₃ NCs were highly stable at room temperature and atmospheric pressure. To test the reusability of the MoS₂/Fe₂O₃ NCs, we repeated the SERS experiment five times with the same

Fig. 4 Detection of Pauly's reagent. a SERS spectra of BPA, *p*-aminobenzene sulfonic acid, NaNO$_3$, and Na$_2$CO$_3$ adsorbed on the MoS$_2$/Fe$_2$O$_3$ NCs. **b** SERS spectrum of *p*-aminobenzene sulfonic acid adsorbed on the MoS$_2$/Fe$_2$O$_3$ NCs. **c** SERS spectra of NaNO$_3$ adsorbed on the MoS$_2$/Fe$_2$O$_3$ NCs. **d** SERS spectrum of Na$_2$CO$_3$ adsorbed on the MoS$_2$/Fe$_2$O$_3$ NCs.

Fig. 5 Sensitivity, stability, and reproducibility of MoS$_2$/Fe$_2$O$_3$ NCs. a SERS spectra of MoS$_2$/Fe$_2$O$_3$ NCs incubated with a BPA aqueous solution at various concentrations. **b** Calibration curve for BPA at 1124 cm^{-1}. **c** SERS spectra of the 10^{-4} M BPA aqueous solution based on the MoS$_2$/Fe$_2$O$_3$ substrate collected at different shelf times. **d** Room temperature magnetic hysteresis curves of the MoS$_2$/Fe$_2$O$_3$ NCs and MoS$_2$ NFs. The inset shows the water dispersibility and magnetic separability of the MoS$_2$/Fe$_2$O$_3$ NCs. **e** SERS spectra of BPA after the self-cleaning test. **f** Corresponding normalized Raman intensities of 1385 cm^{-1} when the SERS substrate was recycled five times for the detection of 10^{-4} M BPA.

sample. After each experiment, the MoS$_2$/Fe$_2$O$_3$ NCs were separated from the solution using a magnet. Figure 5e shows the SERS spectrum of a MoS$_2$/Fe$_2$O$_3$ substrate that

was reused after absorbing the same concentration of BPA; the results indicated that the substrate had good reproducibility. As shown in Fig. 5f, the MoS$_2$/Fe$_2$O$_3$ NC

substrate had excellent SERS activity even after five recycling runs. Although the average Raman intensity decreased slightly, it satisfied the qualitative testing requirements for BPA. These results indicate that the MoS_2/Fe_2O_3 NCs were reproducible and show promise as reusable substrate materials.

Detection in "real-world" samples

To evaluate the application of the MoS_2/Fe_2O_3 NCs, "real-world" samples (lake water and milk) were chosen for detection. As shown in Fig. 6, the characteristic CH wagging peak of BPA at $1124 \, cm^{-1}$ was observed at concentrations as low as 10^{-7} M for these samples, indicating that the MoS_2/Fe_2O_3 NCs could be used for the practical and rapid detection of BPA.

Photocatalytic activity of MoS₂/Fe₂O₃ NCs

The catalytic properties of the pristine MoS_2 NFs, Fe_2O_3 NPs, and MoS_2/Fe_2O_3 NCs were evaluated by performing BPA degradation experiments under UV irradiation. The BPA degradation results for the MoS_2
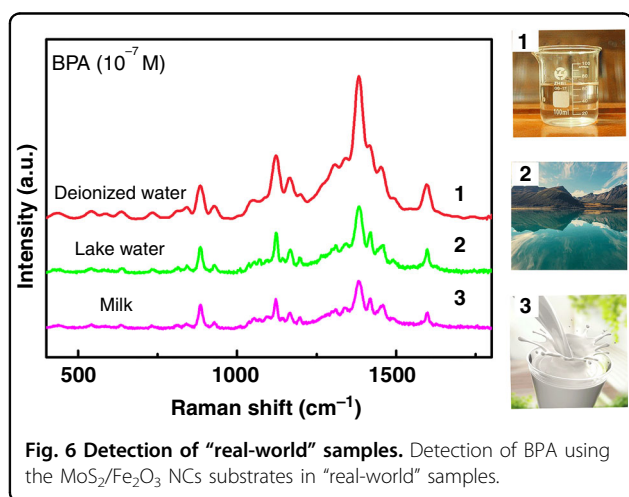
Fig. 6 Detection of "real-world" samples. Detection of BPA using the MoS_2/Fe_2O_3 NCs substrates in "real-world" samples.

NFs, Fe_2O_3 NPs, and MoS_2/Fe_2O_3 NCs samples under UV light are presented in Fig. 7a–c, respectively. For all catalysts, the intensity of the main absorption peak decreased with increasing irradiation time. After 50 min of UV irradiation, the degradation rates of the two pristine photocatalysts (MoS_2 NFs and Fe_2O_3 NPs) were only ~40% and 48%, respectively. Surprisingly, the photocatalytic activity was significantly increased in the presence of the MoS_2/Fe_2O_3 NCs catalyst; in this case, >92% of the present BPA was decomposed after 50 min of irradiation, as shown in Fig. 7c. This degradation rate is significantly higher than those observed with the MoS_2 NFs and Fe_2O_3 NPs.

A related graph showing the dependence of the BPA degradation efficiencies of the MoS_2/Fe_2O_3 NCs and other catalysts on the UV irradiation time is presented in Fig. 8a. We define the degradation efficiency as C/C_0, where C_0 represents the initial BPA concentration (mg/L) and C represents the BPA concentration after the reaction (mg/L). As shown in Fig. 8a, the MoS_2/Fe_2O_3 NCs had better photocatalytic activity than the other catalysts. The photocatalytic efficiency of MoS_2/Fe_2O_3 NCs was as high as 0.02, which was higher than that of pure MoS_2 (0.01) and Fe_2O_3 (0.008). Thus, the MoS_2/Fe_2O_3 NCs has great potential for use in wastewater treatments. Before light irradiation, the photocatalyst and BPA solution were stirred under dark conditions for 10 min to attain an adsorption equilibrium. During this period, the concentration of BPA decreased because of the adsorption of BPA molecules on the photocatalysts. We used the pseudo-first-order mode to investigate the reaction kinetics of BPA degradation. The simplified equation is:

$$-\ln(C/C_0) + kt \qquad (2)$$

where k represents the apparent first-order reaction rate constant[35]. Figure 8b shows the relationship
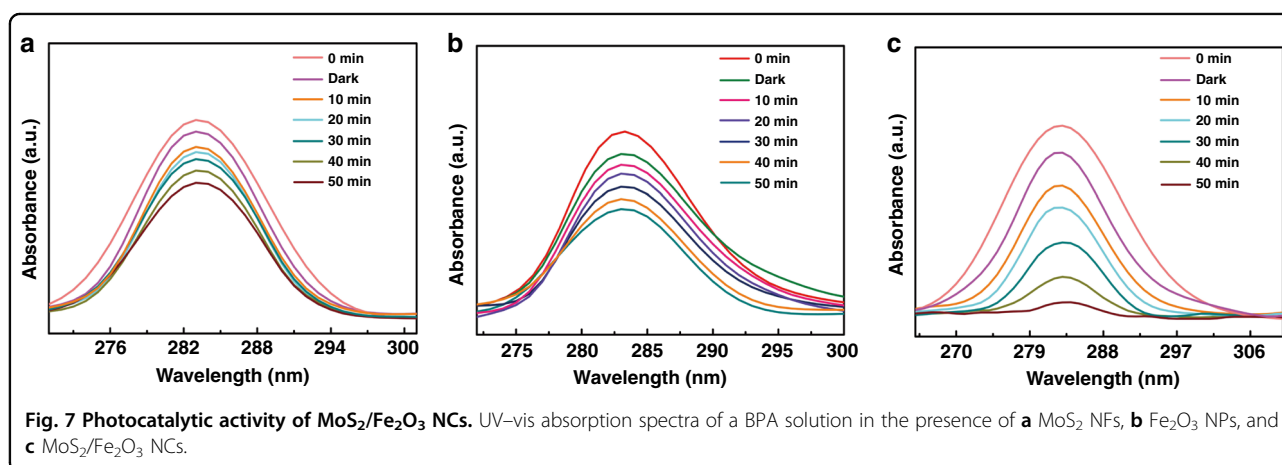
Fig. 7 Photocatalytic activity of MoS₂/Fe₂O₃ NCs. UV–vis absorption spectra of a BPA solution in the presence of **a** MoS_2 NFs, **b** Fe_2O_3 NPs, and **c** MoS_2/Fe_2O_3 NCs.
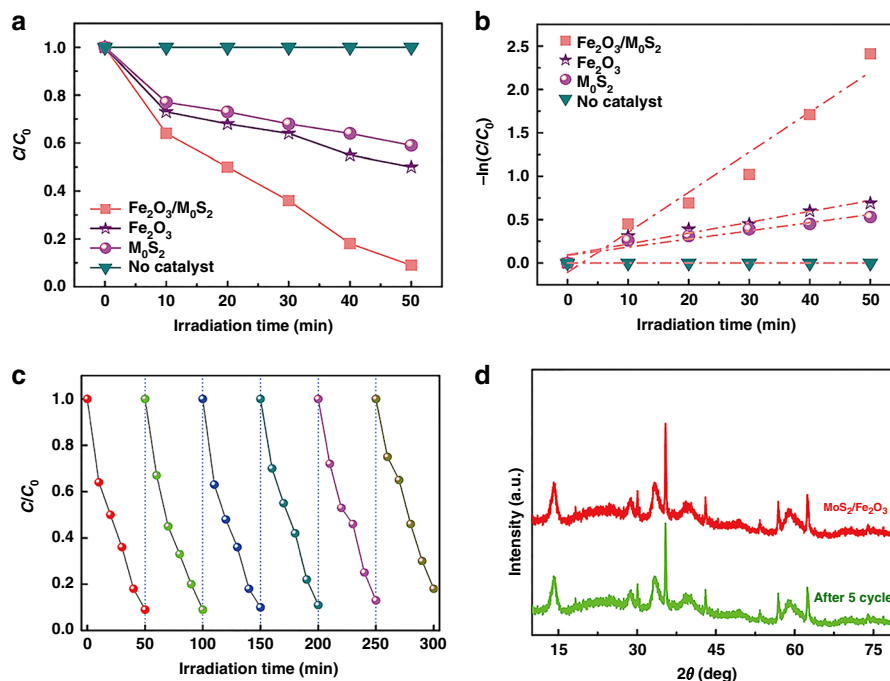
Fig. 8 Photocatalytic activity and stable photoactivity of MoS₂/Fe₂O₃ NCs. a Evolution of the relative concentrations (C/C_0) of BPA with several photocatalysts as a function of irradiation time. **b** Corresponding kinetic plots of the photocatalytic degradation of BPA with the selected photocatalysts. **c** Reusability and stable activity of the MoS₂/Fe₂O₃ NCs after being used for five cycles of the photocatalytic degradation of BPA. **d** XRD pattern of the MoS₂/Fe₂O₃ NCs before and after the fifth cycle.

between $-\ln(C/C_0)$ and the irradiation time for different photocatalysts. The curves could be fitted with a linear relationship, indicating that the degradation kinetics followed a typical first-order reaction. Using Eq. (1), we determined the apparent pseudo-first-order rate constants for the different photocatalysts. The k values of the pristine Fe_2O_3 NPs, MoS_2 NFs, and MoS_2/Fe_2O_3 NCs were calculated to be 0.69, 0.53, and 2.41, respectively. Stable photoactivity under UV light is critical for practical water treatment applications, particularly for composite materials that may lose their coating. We examined the loss of the BPA degradation activity of the MoS_2/Fe_2O_3 NCs by utilizing it for five consecutive cycles under UV light irradiation. No loss of activity was observed (Fig. 8c). As shown in Fig. 8d, the structure of the catalyst was not significantly changed after five consecutive photocatalytic degradation cycles, also suggesting that the Fe_2O_3 nanoparticles could slow down the photocorrosion of MoS_2, thereby efficiently protecting MoS_2. Generally, MoS_2 is prone to photocorrosion due to oxidation of surface sulfions to sulfurs by photoexcited holes. Therefore, the MoS_2/Fe_2O_3 NCs exhibited high stability and excellent anti-photocorrosion properties, showing that this material has promise for use in environmental restoration applications.

Mechanisms of SERS detection and photocatalysis

When the MoS_2/Fe_2O_3 heterojunction system was irradiated with UV light, MoS_2 was excited, generating electron–hole pairs because of its narrow bandgap. The photoinduced electrons moved rapidly from the conduction band (CB) of MoS_2 to that of Fe_2O_3, as shown in Fig. 9. In the MoS_2/Fe_2O_3 NCs, the spatial separation of photoexcited holes and electrons extended the charge-carrier lifetime and hindered the recombination of electron–hole pairs, thereby enhancing the photocatalytic activity. Moreover, the selected transfer of holes from the valence band (VB) of MoS_2 to Fe_2O_3 remarkably weakened the photocorrosion activity. After the carriers of MoS_2 and Fe_2O_3 were generated, the free electrons accumulated in the CB of Fe_2O_3, while photoinduced holes were present in the VB of MoS_2; thus, a high photocatalytic activity was obtained. Effective Z-type electron–hole pair separation and an effective transfer path were achieved, and a strong redox capacity of the photoexcited electron and holes was obtained in the CB and VB, respectively, significantly improving the photocatalytic and SERS activity of the MoS_2/Fe_2O_3 NC heterojunction. Therefore, Fe_2O_3 not only acted as a protective shell for the MoS_2 core by preventing the loss of sulfur but also constructed Z-type junctions that prolonged the lives of photogenerated electrons and holes,
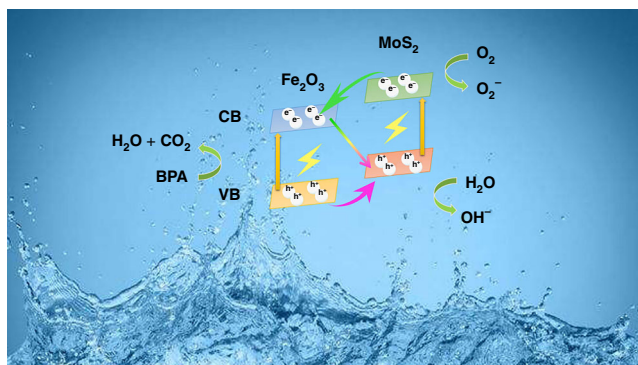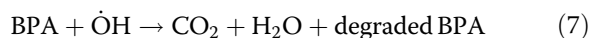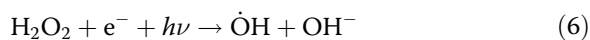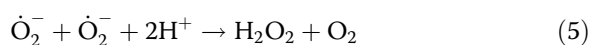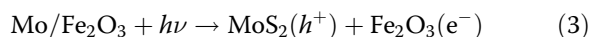
Fig. 9 SERS and photocatalytic mechanisms of MoS₂/Fe₂O₃NCs. Schematic illustration showing the proposed SERS and photocatalytic mechanisms of MoS₂/Fe₂O₃ NCs.

which would significantly enhance the photocatalytic activity and stability. Another reason for the SERS enhancement was the semiconducting nature of MoS₂. Because its surface had S atoms and polar covalent bonds (Mo-S) perpendicular to the surface, this dipole–dipole coupling significantly increased the intensity of the Raman peaks[36]. In addition, because of the large surface-to-volume ratio, there was an abundance of active adsorption sites for gas molecules. The reactions involved in the photocatalytic process are summarized as follows:

$$Mo/Fe_2O_3 + h\nu \rightarrow MoS_2(h^+) + Fe_2O_3(e^-) \qquad (3)$$

$$O_2 + e^- \rightarrow \dot{O}_2^- \qquad (4)$$

$$\dot{O}_2^- + \dot{O}_2^- + 2H^+ \rightarrow H_2O_2 + O_2 \qquad (5)$$

$$H_2O_2 + e^- + h\nu \rightarrow \dot{O}H + OH^- \qquad (6)$$

$$BPA + \dot{O}H \rightarrow CO_2 + H_2O + degraded\,BPA \qquad (7)$$

Conclusion

In summary, a multifunctional material was fabricated by simply depositing Fe₂O₃ NPs onto MoS₂ NFs, which significantly improved its photocatalytic properties and ability to be used as a SERS substrate. In addition, the MoS₂/Fe₂O₃ NCs were successfully recycled. This study is the first to report MoS₂/Fe₂O₃ NCs used as SERS substrates for BPA detection. The MoS₂/Fe₂O₃ NCs had a detection limit of 1×10^{-9} M, along with exhibiting excellent stability. The prepared MoS₂/Fe₂O₃ NCs had higher photocatalytic activity than the MoS₂ NFs and Fe₂O₃ NPs alone. The enhanced photocatalytic activity and SERS activity were attributed to the efficient separation and transfer of electron–hole pairs by the Z-scheme heterojunction system. Therefore, as efficient multifunctional catalysts, MoS₂/Fe₂O₃ NCs are expected to not only replace metal catalysts

for removing organic matter from water and the environment but also pave the way for SERS applications, thereby introducing new methods for chemical and medical detection and for environmental monitoring.

Materials and methods
MoS2 NF preparation

First, 0.5 g H₄MoNa₂O₆ and 0.7 g CH₄N₂S were mixed and stirred in 70 mL of ultrapure water. Then, 0.5 g C₆H₈O₇·H₂O was added until complete dissolution was achieved. The sample was transferred into an 80 mL Teflon-lined hydrothermal autoclave reactor and then placed in a drying box at 240 °C for 24 h. Next, the reaction products were centrifuged with alcohol and ultrapure water and dried at 70 °C.

MoS₂/Fe₂O₃ NC preparation

First, 0.2 g of MoS₂ powder, 0.5 g of H₁₈FeN₃O₁₈, and 0.7 g of H₂NCONH₂ were mixed in 70 mL of ultrapure water. Then, 0.02 g of C₁₈H₂₉NaO₃S were well dispersed in the liquid mixture, stirred in a 60 °C water bath for 35 min, transferred to an 80 mL reactor, and finally placed in a drying box at 90 °C for 12 h. The MoS₂/Fe₂O₃ NCs were washed with absolute ethanol and water to remove possible residuals. The solid powder solid was placed in a drying box and kept dry at 80 °C.

Characterizations

XPS (ESCALAB250X, Thermo Scientific) and X-ray diffraction (XRD, D/Max 3C, Rigaku) were used to study the structural quality. TEM (JEM-2100HR, JEOL) and SEM (JSM-7800F, JEOL) were used to characterize the morphology of the samples. UV–visible absorption spectroscopy (UV-3600, Shimadzu Corporation) and a vibrating sample magnetometer (7407, Lake Shore) were used to characterize the optical and magnetic properties of the samples. Raman spectra were obtained with an Ar⁺-ion laser (inVia Raman, Renishaw).

SERS experiments of BPA

We used the coupling reaction of BPA with Pauly's reagents (*p*-aminobenzene sulfonic acid, HCl, NaNO₃, and Na₂CO₃) to enhance the adhesion of BPA onto the surface of the SERS substrate materials. Please refer to our previous report for the detailed process[37].

SERS experiments of BPA in milk and lake water

Real milk contains fat, protein, vitamins, and other organic ingredients that can interfere with the detection of BPA. Therefore, it is necessary to pretreat the milk sample with BPA. The process is as follows. First, methanol (7 mL) and water (3 mL) were mixed and added to the milk sample (containing 10^{-7} M BPA, 4 mL), and then the mixture was sonicated and centrifuged at 10,000 r.p.m. for 3 min. The upper supernatant was extracted and then dried. This extract was collected in another centrifuge tube and mixed with methanol and water, with the above sonication and centrifugation process being repeated. Finally, the extract was filtered by membrane filters (0.45 and 0.22 μm) for the SERS test. The procedures for the detection and data analysis were the same as those for detecting BPA in water.

We collected lake water from a local source (South Lake in Changchun City). Lake water samples with BPA added were filtered by membrane filters (0.45 and 0.22 μm) before the detection test to avoid interference from other impurities. The test process was consistent with that described above.

Photodegradation experiments

In the degradation process, circulating water was used to ensure that all the tests were performed at room temperature. The photodegradation of BPA under UV light was performed to assess the activity of photocatalysts. One hundred milliliters of an aqueous solution was prepared with 0.001 g of BPA and 0.05 g of Fe₂O₃/MoS₂, MoS₂, or Fe₂O₃ NCs. The test solution was stirred magnetically in a 100-mL beaker. The sample was kept in a dark room for 10 min for the adsorption of BPA molecules on the photocatalysts before being subjected to UV irradiation. During the experiment, the samples were taken at specified times. After each sampling, the catalyst was separated via centrifugation for testing.

Author details
¹Key Laboratory of Functional Materials Physics and Chemistry of the Ministry of Education, Jilin Normal University, 130103 Changchun, People's Republic of China. ²National Demonstration Centre for Experimental Physics Education, Jilin Normal University, 136000 Siping, People's Republic of China. ³Key Laboratory of Preparation and Application of Environmental Friendly Materials, Jilin Normal University, Ministry of Education, 130103 Changchun, People's Republic of China. ⁴College of Science, Changchun University, 130022 Changchun, People's Republic of China. ⁵Changchun Institute of Optics, Fine Mechanics and Physics, Chinese Academy of Sciences, 130103 Changchun, People's Republic of China

Author contributions
M.H. and Y.Q. put forward ideas. M.H. conducted the experiment and wrote the original draft preparation. S.Y., R.S., H.L., and J.Y. participated in the discussion of the experimental data. L.C. provided good advice. M.G. designed the project and also revised and edited the manuscript.

Conflict of interest
The authors declare that they have no conflict of interest.

References
1. Alsbaiee, A. et al. Rapid removal of organic micropollutants from water by a porous β-cyclodextrin polymer. *Nature* **529**, 190–194 (2016).
2. Tao, F. F. & Salmeron, M. In situ studies of chemistry and structure of materials in reactive environments. *Science* **331**, 171–174 (2011).
3. Sarwar, M. et al. Smart-phone, paper-based fluorescent sensor for ultra-low inorganic phosphate detection in environmental samples. *Microsyst. Nanoeng.* **5**, 56 (2019).
4. Guan, Y. & Sun, B. Detection and extraction of heavy metal ions using paper-based analytical devices fabricated via atom stamp printing. *Microsyst. Nanoeng.* **6**, 14 (2020).
5. Le Pivert, M. et al. Direct growth of ZnO nanowires on civil engineering materials: smart materials for supported photodegradation. *Microsyst. Nanoeng.* **5**, 57 (2019).
6. Yousefi, N., Lu, X. L., Elimelech, M. & Tufenkji, N. Environmental performance of graphene-based 3D macrostructures. *Nat. Nanotechnol.* **14**, 107–119 (2019).
7. Kim, J. et al. Uniaxially crumpled graphene as a platform for guided myotube formation. *Microsyst. Nanoeng.* **5**, 53 (2019).
8. Wang, Y. et al. Low sample volume origami-paper-based graphene-modified aptasensors for label-free electrochemical detection of cancer biomarker-EGFR. *Microsyst. Nanoeng.* **6**, 32 (2020).
9. Shan, H. Y. et al. Direct observation of ultrafast plasmonic hot electron transfer in the strong coupling regime. *Light Sci. Appl.* **8**, 9 (2019).
10. Sanjay, B. & Vikas, B. Interfacial nondegenerate doping of MoS₂ and other two-dimensional semiconductors. *ACS Nano* **9**, 2227–2230 (2015).
11. Shi, Y. et al. Hot electron of Au nanorods activates the electrocatalysis of hydrogen evolution on MoS₂ nanosheets. *J. Am. Chem. Soc.* **137**, 7365–7370 (2015).
12. Kang, Y. et al. Plasmonic hot electron induced structural phase transition in a MoS₂ monolayer. *Adv. Mater.* **26**, 6467–6471 (2014).
13. Yao, J. C. et al. AgNPs decorated Mg-doped ZnO nanobroccolis hetero-structure with dramatic SERS activity. *J. Mater. Chem. C* **7**, 8199–8208 (2019).
14. Liu, K. et al. Porous Au–Ag nanospheres with high-density and highly accessible hotspots for SERS analysis. *Nano Lett.* **16**, 3675–3681 (2016).
15. Wang, Y. Q. et al. SERS tags: novel optical nanoprobes for bioanalysis. *Chem. Rev.* **113**, 1391–1428 (2013).
16. Song, Z. L. et al. Alkyne-functionalized superstable graphitic silver nanoparticles for raman imaging. *J. Am. Chem. Soc.* **136**, 13558–13561 (2014).
17. Phan-Quang, G. C., Lee, H. K., Phang, I. Y. & Ling, X. Y. Plasmonic colloidosomes as three-dimensional SERS platforms with enhanced surface area for multi-phase sub-microliter toxin sensing. *Angew. Chem. Int. Ed.* **54**, 9691–9695 (2015).
18. Yang, M. Q., Han, C. & Xu, Y. J. Insight into the effect of highly dispersed MoS₂ versus layer-structured MoS₂ on the photocorrosion and photoactivity of CdS in graphene–CdS–MoS₂ composites. *J. Phys. Chem. C* **119**, 27234–27246 (2015).

19. Zheng, L. X., Han, S. C., Liu, H., Yu, P. P. & Fang, X. S. Hierarchical MoS_2 Nanosheet@TiO_2 Nanotube Array composites with enhanced photocatalytic and photocurrent performances. *Small* **12**, 1527–1536 (2016).

20. Chen, Z. et al. Core-shell MoO_3-MoS_2 nanowires for hydrogen evolution: a functional design for electrocatalytic materials. *Nano Lett.* **11**, 4168–4175 (2011).

21. Yin, D. et al. 2D porous aromatic framework as a novel solid-phase extraction adsorbent for the determination of trace BPA in milk. *Microchim. Acta* **81**, 749–758 (2018).

22. La, M. M. A. et al. Consensus on the key characteristics of endocrine-disrupting chemicals as a basis for hazard identification. *Nat. Rev. Endocrinol.* **16**, 45–57 (2020).

23. Xie, S. Y. et al. Intelligent mesoporous materials for selective adsorption and mechanical release of organic pollutants from water. *Adv. Mater.* **30**, 1800683 (2018).

24. Jia, F., Wang, Q., Wu, J., Li, Y. & Song, S. Two-dimensional molybdenum disulfide as a superb adsorbent for removing Hg^{2+} from water. *ACS Sustain. Chem. Eng.* **5**, 7410–7419 (2017).

25. Yu, J. et al. Smart MoS_2/Fe_3O_4 nano-theranostic for magnetically targeted photothermal therapy guided by magnetic resonance/photoacoustic imaging. *Theranostics* **5**, 931–945 (2015).

26. Liu, X. et al. Facile synthesis of boron-and nitride-doped MoS_2 nanosheets as fluorescent probes for the ultrafast, sensitive, and label-free detection of Hg^{2+}. *Analyst* **140**, 4654–4661 (2015).

27. Valdivia, A., Tweet, D. & Conley, J. Atomic layer deposition of two dimensional MoS_2 on 150 mm substrates. *J. Vac. Sci. Technol. A* **34**, 021515 (2016).

28. Zhou, H. et al. Controlled formation of mixed nanoscale domains of high capacity Fe_2O_3-FeF_3 conversion compounds by direct fluorination. *ACS Nano* **9**, 2530–2539 (2015).

29. Zhu, H. et al. When cubic cobalt sulfide meets layered molybdenum disulfide: a core-shell system toward synergetic electrocatalytic water splitting. *Adv. Mater.* **27**, 4752–4759 (2015).

30. Jiang, J. C. et al. Large-scale synthesis of single-crystalline iron oxide magnetic nanorings. *J. Am. Chem. Soc.* **130**, 16968–16977 (2008).

31. Wang, Z. Q. et al. A platinum oxide decorated amorphous cobalt oxide hydroxide nanosheet array towards alkaline hydrogen evolution. *J. Mater. Chem. A* **6**, 3864–3868 (2018).

32. Yang, S. et al. Monitoring the charge transfer process in a Nd-doped semiconductor based on photoluminescence and SERS. *Technol. Light Sci. Appl.* **9**, 117 (2020).

33. Zheng, Z. H. et al. Semiconductor SERS enhancement enabled by oxygen incorporation. *Nat. Commun.* **8**, 1993 (2017).

34. Chao, Y. F. et al. Self-assembly of flexible free-standing 3D porous MoS_2-reduced graphene oxide structure for high-performance lithium-ion batteries. *Adv. Funct. Mater.* **27**, 1700234 (2017).

35. Islam, S. E., Hang, D. R., Chen, C. H. & Sharma, K. H. Facile and cost-efficient synthesis of quasi 0D/2D ZnO/MoS_2 nanocomposites for highly enhanced visible-light-driven photocatalytic degradation of organic pollutants and antibiotic. *Chem. Eur. J.* **24**, 9305–9315 (2018).

36. Ling, X. et al. Raman enhancement effect on two-dimensional layered materials: graphene, h-BN and MoS_2. *Nano Lett.* **14**, 3033–3040 (2014).

37. Quan, Y. N. et al. ZnO nanoparticles on MoS_2 microflowers for ultrasensitive SERS detection of bisphenol A. *Microchim. Acta* **186**, 593 (2019).